An axially-variant kernel imaging model applied to ultrasound image reconstruction

Mihai I. Florea, Adrian Basarab, Denis Kouamé, Sergiy A. Vorobyov

An Axially Variant Kernel Imaging Model Applied to Ultrasound Image Reconstruction

Mihai I. Florea, *Student Member, IEEE*, Adrian Basarab, *Member, IEEE*, Denis Kouamé, *Member, IEEE*, and Sergiy A. Vorobyov, *Fellow, IEEE*

***Abstract*—Existing ultrasound deconvolution approaches unrealistically assume, primarily for computational reasons, that the convolution model relies on a spatially invariant kernel and circulant boundary conditions. We discard both restrictions and introduce an image formation model applicable to ultrasound imaging and deconvolution based on an axially varying kernel, which accounts for arbitrary boundary conditions. Our model has the same computational complexity as the one employing spatially invariant convolution and has negligible memory requirements. To accommodate the state-of-the-art deconvolution approaches when applied to a variety of inverse problem formulations, we also provide an equally efficient adjoint expression for our model. Simulation results confirm the tractability of our model for the deconvolution of large images. Moreover, in terms of accuracy metrics, the quality of reconstruction using our model is superior to that obtained using spatially invariant convolution.**

***Index Terms*—Axially varying, deconvolution, forward model, kernel, matrix-free, point-spread function, ultrasound.**

I. Introduction

ULTRASOUND imaging is a medical imaging modality widely adopted due to its efficiency, low cost, and safety. These advantages come at the expense of image quality. Consequently, the accurate estimation of the tissue reflectivity function (TRF) from ultrasound images is a subject of active research. Generally, the existing approaches assume that the formation of ultrasound images follows a two-dimensional (2-D) convolution model between the TRF and the system kernel. The convolution model is further constrained for computational reasons to have a spatially invariant kernel and circulant boundary conditions (see, e.g., [1]–[6]).

Pulse-echo emission of focused waves still remains the most widely used acquisition scheme in ultrasound imaging. It consists of sequentially transmitting narrow-focused beams. For each transmission centered at a lateral position, the raw data are used to beamform one radio frequency (RF) signal. Given the repeatability of the process in the lateral direction, the kernels do not vary laterally. However, despite dynamic focusing in reception and time gain compensation, the kernels become wider as we move away from the focal depth, thus, degrading the spatial resolution and motivating the proposed kernel variation model.

Previous works accounted for this variation by assuming kernel invariance over local regions and performing deconvolution blockwise (e.g., [7]). Very recently, ultrasound imaging convolution models with continuously varying kernels were proposed in [8] and [9]. However, the model presented in [8] makes the overly restrictive assumption that the spatially varying kernel is obtained from a constant reference kernel modulated by the exponential of a fixed discrete generator scaled by the varying kernel center image coordinates. Therefore, it does not take into account the depth-dependent spatial-resolution degradation explained previously. On the other hand, the deconvolution method proposed in [9] has an iteration complexity proportional to the cube of the number of pixels in the image, limiting its applicability to very small images.

The contributions of this letter are as follows.

1) We propose a novel axially variant kernel ultrasound image formation model (see Section III).
2) Our model is linear and may be implemented as a matrix. However, the matrix form does not scale because its complexity is proportional to the square of the number of pixels in the image. Therefore, we provide an efficient matrix-free implementation of axially varying convolution that entails the same computational cost as spatially invariant convolution (see Section III-B).
3) The deconvolution problem is ill-posed and many deconvolution models can only be solved approximately using proximal-splitting methods (see [10] and [11] and references therein) that compute the gradient of a data-fidelity term at every iteration. The data-fidelity gradient expression includes calls to both the model operator and its adjoint. We express this adjoint operator in a form of equal complexity to that of the forward model operator (see Section IV).
4) We confirm using simulation results that deconvolution with our model is tractable even for large images and produces results superior to those obtained by using the spatially invariant model (see Section V).

II. Notation

In this letter, images (ultrasound images and TRFs) are vectorized in column-major order but referenced in 2-D form. For

M. I. Florea and S. A. Vorobyov are with the Department of Signal Processing and Acoustics, Aalto University, Aalto FI-00076, Finland (e-mail: mihai.florea@aalto.fi; sergiy.vorobyov@aalto.fi).

A. Basarab and D. Kouamé are with the IRIT, CNRS UMR 5505, University of Toulouse, Toulouse 31062, France (e-mail: basarab@irit.fr; kouame@irit.fr).

Digital Object Identifier 10.1109/LSP.2018.2824764

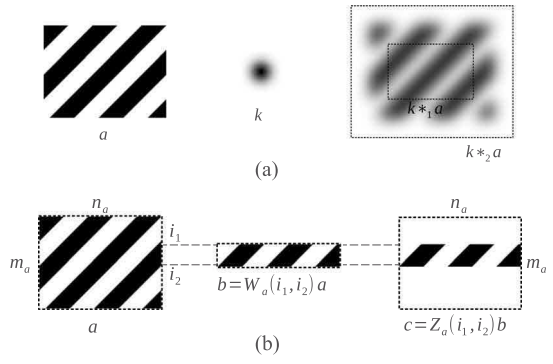

Fig. 1. (a) Convolving test image $\boldsymbol{a}$ with a Gaussian kernel $\boldsymbol{k}$. The inner rectangle represents valid convolution, whereas the outer one marks full convolution. (b) Applying the full-width window operator, followed by a full-width zero-padding operator on test image $\boldsymbol{a}$. Here, black and white correspond to values of 1 and 0, respectively. Kernel $\boldsymbol{k}$ is displayed after min–max normalization.

instance, image $\boldsymbol{v} \in \mathbb{R}^{m_v n_v}$ corresponds to an $m_v \times n_v$ 2-D image and has the pixel value at coordinates (i, j) given by $v_{m_v(j-1)+i}$. However, for clarity of exposition, we denote it as a 2-D object $\boldsymbol{v} \in \mathbb{R}^{m_v \times n_v}$, with the pixel value at location (i, j) given by $\boldsymbol{v}_{i,j}$. Bold marks this artificial indexing. Similarly, linear operators are matrices but referred to as 4-D tensors, e.g., $\boldsymbol{O} : \mathbb{R}^{m_v \times n_v} \to \mathbb{R}^{m_w \times n_w}$ denotes $\boldsymbol{O} \in \mathbb{R}^{m_v n_v \times m_w n_w}$.

In the sequel, we define several classes of linear operators that constitute the mathematical building blocks of our proposed model and its analysis. Note that these are more general than normal linear operators because their dimensions not only depend on those of their parameters but also on the dimensions of their arguments.

A. Convolution Operators

For all $m_k, n_k \geq 1$, all kernels $\boldsymbol{k} \in \mathbb{R}^{m_k \times n_k}$, and all $m_a \geq m_k$, $n_a \geq n_k$, we define the linear operators $\boldsymbol{\mathcal{C}}_1(\boldsymbol{k})$ and $\boldsymbol{\mathcal{C}}_2(\boldsymbol{k})$ as

$$\boldsymbol{\mathcal{C}}_1(\boldsymbol{k})\boldsymbol{a} \stackrel{\text{def}}{=} \boldsymbol{k} *_1 \boldsymbol{a}, \quad \boldsymbol{\mathcal{C}}_2(\boldsymbol{k})\boldsymbol{a} \stackrel{\text{def}}{=} \boldsymbol{k} *_2 \boldsymbol{a}$$

for all $\boldsymbol{a} \in \mathbb{R}^{m_a \times n_a}$, where operations $*_1$ and $*_2$ denote (discrete) valid convolution and full convolution, respectively, defined as

$$(\boldsymbol{k} *_1 \boldsymbol{a})_{i,j} \stackrel{\text{def}}{=} \sum_{p=1}^{m_k} \sum_{q=1}^{n_k} \boldsymbol{k}_{p,q} \boldsymbol{a}_{i-p+m_k, j-q+n_k}$$
$$i \in \{1, \ldots, m_a - m_k + 1\}, \quad j \in \{1, \ldots, n_a - n_k + 1\}$$

$$(\boldsymbol{k} *_2 \boldsymbol{a})_{i,j} \stackrel{\text{def}}{=} \sum_{p=p_i}^{\bar{p}_i} \sum_{q=q_j}^{\bar{q}_j} \boldsymbol{k}_{p,q} \boldsymbol{a}_{i-p+1, j-q+1}$$
$$i \in \{1, \ldots, m_a + n_k - 1\}, \quad j \in \{1, \ldots, n_a + n_k - 1\}$$
$$p_i = \max\{1, i - m_a + 1\}, \quad \bar{p}_i = \min\{i, m_k\}$$
$$q_j = \max\{1, j - n_a + 1\}, \quad \bar{q}_j = \min\{j, n_k\}.$$

The difference between the two forms of convolution is exemplified in Fig. 1(a). Valid convolution is thereby the subset of full convolution where every output pixel is expressed using the entire kernel $\boldsymbol{k}$.

B. Auxiliary Operators

For conciseness, we also introduce the following auxiliary operators. None involve any computation in practice.

Let the rotation operator $\boldsymbol{\mathcal{R}}(\boldsymbol{k})$ be given by

$$(\boldsymbol{\mathcal{R}}(\boldsymbol{k}))_{i,j} \stackrel{\text{def}}{=} \boldsymbol{k}_{m_k - i + 1, n_k - j + 1}$$
$$i \in \{1, \ldots, m_k\}, \quad j \in \{1, \ldots, n_k\}.$$

To further simplify the notation, we denote the exception index set $\mathcal{I}(a, b, c) \stackrel{\text{def}}{=} \{1, \ldots, c\} \backslash \{a, \ldots, b\}$ for all $1 \leq a \leq b \leq c$. The full-width window and zero-padding operators are defined as

$$(\boldsymbol{\mathcal{W}}_s(i_1, i_2)\boldsymbol{a})_{i,j} \stackrel{\text{def}}{=} \boldsymbol{a}_{i+i_1, j}, \quad i \in \{0, \ldots, i_2 - i_1\}$$

$$(\boldsymbol{\mathcal{Z}}_s(i_1, i_2)\boldsymbol{a})_{i,j} \stackrel{\text{def}}{=} \begin{cases} \boldsymbol{a}_{i-i_1, j}, & i \in \{i_1, \ldots, i_2\} \\ 0, & i \in \mathcal{I}(i_1, i_2, m_s) \end{cases}$$

where $j \in \{1, \ldots, n_s\}$ and index $s \in \{t, p\}$ stands for image size quantities m_t, m_p, n_t, and n_p. Their effect on a test image is shown in Fig. 1(b).

III. Axially Variant Kernel Based Ultrasound Imaging Model

We propose the following image formation model:

$$\boldsymbol{y} = \boldsymbol{H}\boldsymbol{P}\boldsymbol{x} + \boldsymbol{n} \tag{1}$$

where $\boldsymbol{x}, \boldsymbol{y}, \boldsymbol{n} \in \mathbb{R}^{m_t \times n_t}$ denote the TRF to be recovered, the observed RF image, and the independent identically distributed additive white Gaussian noise (AWGN), respectively.

A. Padding

Operator $\boldsymbol{P} : \mathbb{R}^{m_t \times n_t} \to \mathbb{R}^{m_p \times n_p}$ pads the TRF with a boundary of width n_r and height m_r, yielding an image of size $m_p = m_t + 2m_r$ times $n_p = n_t + 2n_r$. Padding in our ultrasound imaging model allows us to reconstruct a TRF of the same size as the observed RF image. To this end, we must simulate the effects that the surrounding tissues have on the imaged tissues. Padding is an estimation of the surrounding tissues using information from the imaged TRF. This estimation only affects the border of the reconstructed TRF. If this border information is not required, the reconstructed TRF can simply be cropped accordingly. The addition of padding to our model brings the advantage of accommodating both options.

For computational reasons, $\boldsymbol{P}$ is assumed linear and separable along the dimensions of the image. Separability translates to $\boldsymbol{P} = \boldsymbol{P}_m \boldsymbol{P}_n$. Here, $\boldsymbol{P}_m$ pads every column of the image independently by applying the 1-D padding (linear) operator $\boldsymbol{\mathcal{P}}(m_t, m_r)$. Consequently, when $n_t = 1$ and $n_r = 0$, operators $\boldsymbol{P}$ and $\boldsymbol{\mathcal{P}}(m_t, m_r)$ are equivalent. The row component $\boldsymbol{P}_n$ treats every row as a column vector, applies $\boldsymbol{\mathcal{P}}(n_t, n_r)$ to it, and turns the result back into a row.

Padding, either in 1-D or 2-D, can be performed without explicitly deriving an operator matrix. However, the matrix form facilitates the formulation of the corresponding adjoint operator. Common matrix forms of operator $\boldsymbol{\mathcal{P}}(m_t, n_t)$ are shown in Fig. 2 for $m_t = 10$ and $m_r = 3$. These examples demonstrate that the matrix form of $\boldsymbol{\mathcal{P}}(m_t, m_r)$ can be easily generated programmatically and, due to its sparsity, can be stored in memory

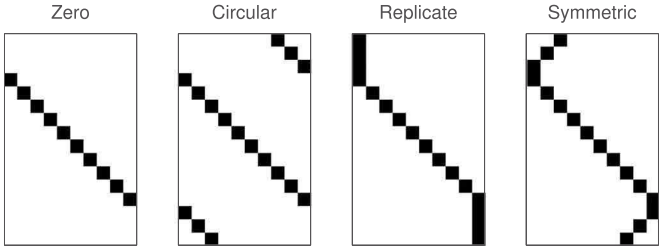

Fig. 2. Common matrix forms of 1-D padding operator $\boldsymbol{\mathcal{P}}(10, 3)$. Black denotes a value of 1 and white denotes 0.

even for very large values of m_t and m_r. These properties extend to the matrix form of the 2-D padding operator $\boldsymbol{P}$ by virtue of the following result.

Theorem 1: Padding operator $\boldsymbol{P}$ can be obtained programatically in the form of a sparse matrix as

$$\boldsymbol{P} = \boldsymbol{\mathcal{P}}(n_t, n_r) \otimes \boldsymbol{\mathcal{P}}(m_t, m_r)$$

where $\otimes$ denotes the Kronecker product.

Proof. See [12, Appendix A]. ■

B. Axially Varying Convolution

Linear operator $\boldsymbol{H}$: $\mathbb{R}^{m_p \times n_p} \rightarrow \mathbb{R}^{m_t \times n_t}$ performs the axially variant kernel convolution. We define it as the operation whereby each *row* $i_h \in \{1, \ldots, m_t\}$ of the output image is obtained by the valid convolution between the kernel pertaining to that row $\boldsymbol{k}(i_h) \in \mathbb{R}^{m_k \times n_k}$, where $m_k = 2m_r + 1$ and $n_k = 2n_r + 1$, and the corresponding patch in the input (padded) TRF. The auxiliary operators defined in Section II enable us to write $\boldsymbol{H}$ as a sum of linear operators based on the observation that the concatenation of the output rows has the same effect as the summation of the rows appropriately padded with zeros. Analytically, this translates to

$$\boldsymbol{H} = \sum_{i_h=1}^{m_t} \boldsymbol{\mathcal{Z}}_t(i_h, i_h) \boldsymbol{\mathcal{C}}_1(\boldsymbol{k}(i_h)) \boldsymbol{\mathcal{W}}_p(i_h, i_h + 2m_r). \tag{2}$$

In matrix form, operator $\boldsymbol{H}$ would need to store $m_p n_p m_t n_t$ coefficients and its invocation would entail an equal number of multiplications. Its complexity would, thus, be greater than the square of the number of pixels in the image, limiting its applicability to medium-sized images. Using the matrix-free expression in (2), operator $\boldsymbol{H}$ performs $m_k n_k m_t n_t$ multiplications and has negligible memory requirements. Therefore, in ultrasound imaging, the matrix-free representation is not only vastly superior to its matrix counterpart (because the kernel is much smaller than the image), but also has the same computational complexity as the spatially invariant convolution operation (excluding the unrealistic circulant boundary case).

Unlike the forward model which, by utilizing operators $\boldsymbol{H}$ and $\boldsymbol{P}$, can be computed exactly with great efficiency, many deconvolution models can only be solved approximately using proximal-splitting methods that optimize an objective containing a data-fidelity term $\phi(\boldsymbol{HPx} - \boldsymbol{y})$. These methods employ at every iteration the gradient of the data-fidelity term, given by

$$\nabla(\phi(\boldsymbol{HPx} - \boldsymbol{y})) = \boldsymbol{P}^T \boldsymbol{H}^T (\nabla\phi)(\boldsymbol{HPx} - \boldsymbol{y}). \tag{3}$$

Note that, under our AWGN assumption, ϕ is the square of the ℓ_2-norm but the results in this letter may be applied to other additive noise models.

The gradient expression in (3) depends on $\boldsymbol{H}$ and $\boldsymbol{P}$ as well as their adjoints. In the following, we derive computationally efficient expressions for adjoint operators $\boldsymbol{H}^T$ and $\boldsymbol{P}^T$.

IV. Adjoint of Model Operator

By taking the adjoint in (2), we get

$$\boldsymbol{H}^T = \sum_{i_h=1}^{m_t} (\boldsymbol{\mathcal{W}}_p(i_h, i_h + 2m_r))^T (\boldsymbol{\mathcal{C}}_1(\boldsymbol{k}(i_h)))^T (\boldsymbol{\mathcal{Z}}_t(i_h, i_h))^T.$$

To obtain a matrix-free representation of $\boldsymbol{H}^T$, we need the corresponding matrix-free expressions for the adjoints of the convolution and auxiliary operators. First, it trivially holds that the window operator and the corresponding zero-padding operator are mutually adjoint expressed as

$$(\boldsymbol{\mathcal{W}}_s(i_1, i_2))^T = \boldsymbol{\mathcal{Z}}_s(i_1, i_2). \tag{4}$$

The adjoint of valid convolution can be linked to full convolution as follows.

Theorem 2: The adjoint of valid convolution is full correlation (convolution with the rotated kernel), namely

$$(\boldsymbol{\mathcal{C}}_1(\boldsymbol{k}))^T = \boldsymbol{\mathcal{C}}_2(\boldsymbol{\mathcal{R}}(\boldsymbol{k})).$$

Proof. See [12, Appendix B]. ■

Theorem 2 and (4) yield a matrix-free expression for $\boldsymbol{H}^T$ in the form of

$$\boldsymbol{H}^T = \sum_{i_h=1}^{m_t} \boldsymbol{\mathcal{Z}}_p(i_h, i_h + 2m_r) \boldsymbol{\mathcal{C}}_2(\boldsymbol{\mathcal{R}}(\boldsymbol{k}(i_h))) \boldsymbol{\mathcal{W}}_t(i_h, i_h). \tag{5}$$

Therefore, operators $\boldsymbol{H}$ and $\boldsymbol{H}^T$ have equal computational complexity. Moreover, they exhibit two levels of parallelism. The convolution operators themselves are fully parallel and the computations pertaining to each row i_h can be performed concurrently. Thus, in matrix-free from, both operators benefit from parallelization in the same way as their matrix counterparts.

The adjoint of the padding operator $\boldsymbol{P}^T$ can be obtained either directly through sparse matrix transposition or by applying transposition in Theorem 1 as

$$\boldsymbol{P}^T = (\boldsymbol{P})^T = (\boldsymbol{\mathcal{P}}(n_t, n_r))^T \otimes (\boldsymbol{\mathcal{P}}(m_t, m_r))^T. \tag{6}$$

Finally, note that whereas the column-major order assumption can be made without loss of generality for operator $\boldsymbol{H}$, it is not the case for the padding operator $\boldsymbol{P}$. In particular, the row-major vectorization assumption reverses the terms in the Kronecker product.

V. Experimental Results

We have tested our model on a simulated ultrasound image deconvolution problem. The ground truth TRF, as shown in Fig. 3(a), was computed by interpolating to a grid Gaussian distributed random scatterers with standard deviations (SDs) determined by a pixel intensity map (see the kidney phantom from the Field II simulator [13], [14]). The map is a patch from an optical scan of human kidney tissue. The TRF is $m_t = 2480$ by $n_t = 480$ pixels in size, corresponding to 94 mm $\times$ 95 mm.

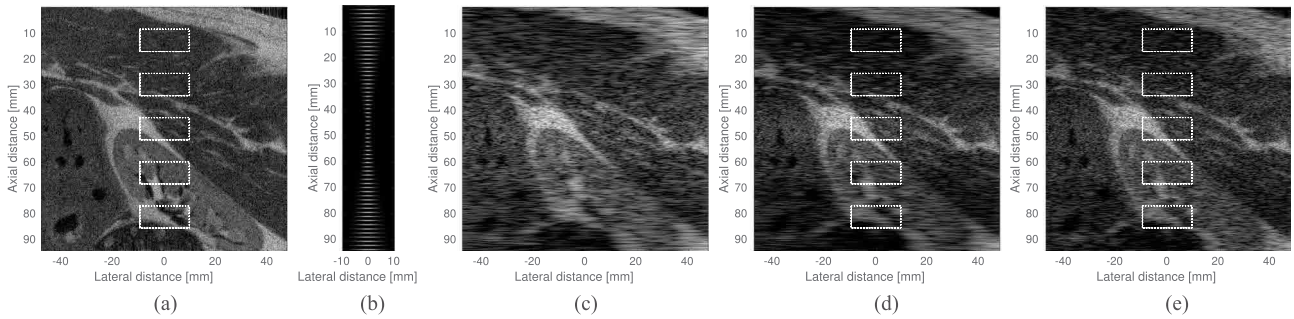

Fig. 3. (a) Ground truth (in B-mode) of the TRF. (b) Demodulated kernels $\boldsymbol{k}(i_h)$ for 20 depths at regularly spaced intervals of 2 mm. (c) Observed B-mode image simulated following the proposed axially variant convolution model. (d) AI deconvolution result, IR in B-mode, obtained with a fixed kernel equal to $\boldsymbol{k}(m_t/2)$ (the center kernel of the AV model). (e) AV deconvolution result, VR in B-mode, using our model. All the images are displayed using a dynamic range of 40 dB. White rectangles mark the patches used in computing the quality metrics.

More TRFs and their corresponding simulation results can be found in [12].

For every row $i_h \in \{1, \ldots, m_t\}$, we have defined the kernel $\boldsymbol{k}(i_h)$ in (2) as

$$\boldsymbol{k}(i_h)_{i,j} = \rho_{\mu_z,\sigma_z}(i)\rho_{\mu_x,\sigma_x(i_h)}(j)\cos\left(2\pi f_0/f_s(i-\mu_z)\right)$$

where $\rho_{\mu,\sigma}(x)$ is a normalized Gaussian window, given by $\rho_{\mu,\sigma}(x) = \frac{1}{\sqrt{2\pi}\sigma}\exp\left(-\frac{(x-\mu)^2}{2\sigma^2}\right)$, and parameters μ_z and μ_x are the center coordinates of the kernel. Axial SD was set to $\sigma_z = \sigma_1$ and lateral SD to $\sigma_x(i_h) = \sqrt{((2i_h)/m_t - 1)^2(\sigma_2^2 - \sigma_1^2) + \sigma_1^2}$, with $\sigma_1 = m_r/3$ and $\sigma_2 = n_r/3$. Here, $f_0 = 3$ MHz and $f_s = 20$ MHz are the ultrasound central and sampling frequencies, respectively. The depth-dependent width variation of the kernel simulates the lateral spatial-resolution degradation when moving away from the focus point, located in this experiment at the center of the image (47 mm from the probe). The envelopes of these kernels at regular intervals across the image are shown in Fig. 3(b). We chose symmetric padding, as illustrated in Fig. 2, because it is more realistic than circular padding and zero padding and, by using a larger number of pixels from the TRF, more robust to noise than replicate padding. A small amount of noise was added such that the signal-to-noise ratio is 40 dB. The ultrasound image produced from the TRF using our forward model in (1) is shown in Fig. 3(c).

To estimate the TRF, we have considered an elastic net [15] regularized least squares (based on the AWGN assumption) deconvolution model

$$\min_{\boldsymbol{x}} \frac{1}{2}\|\boldsymbol{HPx} - \boldsymbol{y}\|_2^2 + \lambda_1\|\boldsymbol{x}\|_1 + \frac{\lambda_2}{2}\|\boldsymbol{x}\|_2^2$$

with manually tuned parameters $\lambda_1 = 2e-3$ and $\lambda_2 = 1e-4$. For deconvolution, we have employed the accelerated composite gradient method (ACGM) [16], [17] on account of its low resource usage, applicability, adaptability, and near-optimal linear-convergence rate on elastic net regularized optimization problems.

Every iteration of ACGM is dominated by the computationally intensive data-fidelity gradient function $\nabla f(\boldsymbol{x}) = \boldsymbol{P}^T\boldsymbol{H}^T(\boldsymbol{HPx} - \boldsymbol{y})$. All other calculations performed by ACGM are either negligible when compared to $\nabla f(\boldsymbol{x})$ or can be reduced to subexpressions of $\nabla f(\boldsymbol{x})$.

Due to the efficient matrix-free expressions of $\boldsymbol{H}$ in (2) and $\boldsymbol{H}^T$ in (5) as well as the sparse matrix implementation of $\boldsymbol{P}$ and $\boldsymbol{P}^T$ (easily precomputed using Theorem 1 and (6), respectively), deconvolution with our model entails the same computational cost as with a fixed-kernel model.

TABLE I
ACCURACY METRICS COMPUTED FOR FIVE PATCHES IN THE RECONSTRUCTED IMAGES IR AND VR

Patch center row	IR NRMSE	IR MSSIM	VR NRMSE	VR MSSIM
13 mm	0.0972	99.45%	0.0291	99.84%
30 mm	0.0978	99.43%	0.0317	99.81%
47 mm	0.1571	96.55%	0.1194	97.01%
64 mm	0.1088	98.74%	0.0635	99.06%
81 mm	0.1267	97.72%	0.0888	98.05%

The result of axially invariant (AI) deconvolution, IR, is shown in Fig. 3(d), and using our axially variant (AV) model, VR, in Fig. 3(e), both after 150 iterations. The normalized root-mean-square error (NRMSE) and the mean image structural similarity (MSSIM) [18] accuracy metrics were computed for five patches in IR and VR after Gaussian normalization and envelope detection. The values are listed in Table I.

Our approach achieves almost perfect low-frequency reconstruction across the TRF. The gain in reconstruction quality is evident, especially in the upper and lower extremities, as can be discerned both empirically from Fig. 3 as well as from the accuracy metric discrepancy in the corresponding patches (see Table I), particularly the NRMSE. Interestingly, even though the two models differ only slightly at the center of the image, our model performs better in that region as well.

VI. CONCLUSION

In this letter, we have proposed an axially varying convolution forward model for ultrasound imaging. The physics of ultrasound image formation as well as our deconvolution simulation results show the superiority of our model over the traditional fixed-kernel model.

Our matrix-free formulae for the adjoints of the convolution and auxiliary operators, necessary for the implementation of deconvolution using proximal-splitting techniques, also constitute a solid theoretical foundation for deconvolution methodologies using more sophisticated models, particularly those where the kernel also varies along the lateral direction. Furthermore, our theoretical results and methodology are not restricted to ultrasound imaging only and may be extrapolated to other imaging modalities and applications as well.

REFERENCES

[1] J. Ng, R. Prager, N. Kingsbury, G. Treece, and A. Gee, "Wavelet restoration of medical pulse-echo ultrasound images in an EM framework," *IEEE Trans. Ultrason., Ferroelect., Freq. Control*, vol. 54, no. 3, pp. 550–568, Mar. 2007.

[2] R. Rangarajan, C. V. Krishnamurthy, and K. Balasubramaniam, "Ultrasonic imaging using a computed point spread function," *IEEE Trans. Ultrason., Ferroelect., Freq. Control*, vol. 55, no. 2, pp. 451–464, Feb. 2008.

[3] H.-C. Shin *et al.*, "Sensitivity to point-spread function parameters in medical ultrasound image deconvolution," *Ultrasonics*, vol. 49, no. 3, pp. 344–357, 2009.

[4] M. Alessandrini *et al.*, "A restoration framework for ultrasonic tissue characterization," *IEEE Trans. Ultrason., Ferroelect., Freq. Control*, vol. 58, no. 11, pp. 2344–2360, Nov. 2011.

[5] C. Dalitz, R. Pohle-Frohlich, and T. Michalk, "Point spread functions and deconvolution of ultrasonic images," *IEEE Trans. Ultrason., Ferroelect., Freq. Control*, vol. 62, no. 3, pp. 531–544, Mar. 2015.

[6] N. Zhao, A. Basarab, D. Kouamé, and J.-Y. Tourneret, "Joint segmentation and deconvolution of ultrasound images using a hierarchical Bayesian model based on generalized Gaussian priors," *IEEE Trans. Image Process.*, vol. 25, no. 8, pp. 3736–3750, Aug. 2016.

[7] J. G. Nagy and D. P. O'Leary, "Restoring images degraded by spatially variant blur," *SIAM J. Sci. Comput.*, vol. 19, no. 4, pp. 1063–1082, Jul. 1998.

[8] O. V. Michailovich, "Non-stationary blind deconvolution of medical ultrasound scans," in *Proc. Int. Soc. Opt. Eng.*, Bellingham, WA, USA, Mar. 2017, Paper 101391C.

[9] L. Roquette, M. M. J.-A. Simeoni, P. Hurley, and A. G. J. Besson, "On an analytical, spatially-varying, point-spread-function," in *Proc. 2017 IEEE Int. Ultrasound Symp.*, Sep. 2017, Washington, DC, USA, pp. 1–4.

[10] P. L. Combettes and J.-C. Pesquet, "Proximal splitting methods in signal processing," in *Fixed-Point Algorithms for Inverse Problems in Science and Engineering*. New York, NY, USA: Springer-Verlag, 2011, pp. 185–212.

[11] N. Parikh *et al.*, "Proximal algorithms," *Found. Trends Optim.*, vol. 1, no. 3, pp. 127–239, 2014.

[12] M. I. Florea, A. Basarab, D. Kouamé, and S. A. Vorobyov, "An axially-variant kernel imaging model for ultrasound image reconstruction," *arXiv:1801.08479*, 2018.

[13] J. A. Jensen, "Field: A program for simulating ultrasound systems," *Med. Biol. Eng. Comput.*, vol. 34, pp. 351–353, 1996.

[14] J. A. Jensen and N. B. Svendsen, "Calculation of pressure fields from arbitrarily shaped, apodized, and excited ultrasound transducers," *IEEE Trans. Ultrason., Ferroelect., Freq. Control*, vol. 39, no. 2, pp. 262–267, Mar. 1992.

[15] H. Zou and T. Hastie, "Regularization and variable selection via the elastic net," *J. Roy. Statist. Soc. B, Methodol.*, vol. 67, no. 2, pp. 301–320, 2005.

[16] M. I. Florea and S. A. Vorobyov, "An accelerated composite gradient method for large-scale composite objective problems," arXiv:1612.02352, Apr. 16, 2018.

[17] M. I. Florea and S. A. Vorobyov, "A generalized accelerated composite gradient method: Uniting Nesterov's fast gradient method and FISTA," arXiv:1705.10266, Apr. 16, 2018.

[18] Z. Wang, A. C. Bovik, H. R. Sheikh, and E. P. Simoncelli, "Image quality assessment: From error visibility to structural similarity," *IEEE Trans. Image Process.*, vol. 13, no. 4, pp. 600–612, Apr. 2004.